Supporting Information

Simultaneous enhancement of piezoelectricity and Curie temperature in KNN-based ceramics via multiple formula solid-solution

Hongjiang Li, Ning Chen, Jie Xing, Wenbin Liu, Zhi Tan*, Hao Chen, Manjing Tang, Mingyue Mo, Jianguo Zhu*

College of Materials Science and Engineering, Sichuan University, Chengdu, Sichuan, 610064, China.

1. Experimental section

1.1. Design of *x* KNN_1+KNN_2+KNN_3 ceramics

The ratio of the three components, KNN_1, KNN_2, and KNN_3, can be set through several parameters.

(a) On the one hand, the polar nanoregions (PNRs) of lead-free piezoceramics can promote domain switching because of their easy response to an electric field; on the other hand, it is difficult to completely re-orientate the PNRs along the electric field. Therefore, the PNRs of lead-free piezoceramics are a double-edged "sword".

(b) The existence of PNRs makes the orientation of ferroelectric domains more chaotic, thereby affecting the ferroelectric long-range order. When the content of PNRs is reduced, ferroelectric domains can be arranged more orderly, enhancing the ferroelectric properties of the material and thereby increasing the Curie temperature (T_C). At the same time, PNRs contribute positively to the piezoelectric performance to a certain extent. Reducing their content weakens the local polarization and strain response, resulting in a decrease in the piezoelectric coefficient d_{33} value.

(c) The Ta and Nb have a similar distribution of electrons outside the nuclei of the

* Corresponding author:
E-mail address: tanzhi0838@scu.edu.cn (Zhi Tan), nic0400@scu.edu.cn (Jianguo Zhu)

atoms, and Ta replaces Sb which contributes to the long-range ferroelectric ordering.

To sum up, in KNN-based ceramics, improving the ferroelectric long-range order can increase T_C, and appropriate content of PNRs can optimize the piezoelectric coefficients (d_{33}) value. Therefore, it is necessary to maximize the local disorder while maintaining the well-constructed macroscopic ferroelectricity to achieve optimal material performance. In this work, we introduce more types of elements that are doped while maintaining the total amount of doping by changing the amount of KNN_1. This is conducive to a local disordered structure and thereby leads to a high dielectric constant. On the other hand, the Ta and Nb have a similar distribution of electrons outside the nuclei of the atoms, and Ta replaces Sb which contributes to the long-range ferroelectric ordering by introducing KNN_1 and thereby increasing T_C. The choice of KNN_1 ratios has a significant impact on the piezoelectric properties of the ceramic. For instance, different ratios can influence the lattice distortion, domain engineering, polymorphic phase boundaries, and PNRs of KNN-based ceramics. This, in turn, affects the piezoelectric coefficients, dielectric properties, and mechanical strength of the material.

1.2. Preparation of *x* KNN_1+KNN_2+KNN_3 ceramics

The *x* $[0.957(K_{0.48}Na_{0.52})Nb_{0.95}Ta_{0.06}O_3$-$0.04(Bi_{0.5}Na_{0.5})ZrO_3$-$0.003BiFeO_3/0.004LiF]^1$ + (1-*x*)/2 $[0.955(K_{0.5}Na_{0.5})(Nb_{0.965}Sb_{0.035})O_3$-$0.045(Bi_{0.94}In_{0.06})_{0.5}Na_{0.5}ZrO_3$-$0.0015Fe_2O_3]^2$ + (1-*x*)/2 $[0.96(K_{0.4}Na_{0.6})Nb_{0.96}Sb_{0.04}O_3$-$0.04(Bi_{0.45}Sm_{0.05})Na_{0.5}ZrO_3]^3$ (*x* KNN_1+KNN_2+KNN_3) ceramics are produced by conventional roll forming technology. The analytically pure K_2CO_3 (99%), Na_2CO_3 (99.8%), Nb_2O_5 (99.95%), Bi_2O_3 (99.999%), ZrO_2 (99%), Fe_2O_3 (99.99%), Ta_2O_5 (99.99%), Sb_2O_3 (99.99%), Sm_2O_3 (99.9%), In_2O_3 (99.99%), and LiF (99.99%) are obtained from Sinopharm Chemical Reagent Co. Ltd., China. Firstly, the analytical grade reagents of high-purity raw materials are mixed by ball milling in a zirconia ball media and anhydrous ethanol solution for 15 to 20 h. Then, the KNN_1, KNN_2, and KNN_3 powders are calcined at 800 to 950 °C for 6 h. The KNN_1, KNN_2, and KNN_3 powders are weighed according to the stoichiometric formula of *x* KNN_1+KNN_2+KNN_3

and mixed in ethanol using zirconia balls for 15 to 20 h. The *x* KNN_1+KNN_2+KNN_3 powders are milled with polyvinyl alcohol (PVA) colloid in a specific mass ratio (*e.g.* 100 g powder corresponds to 6 g PVA). The PVA-mixed powders are pressed into plates with a diameter of 8-10 mm and a thickness of 0.18-0.20 mm using the roll-forming process. Finally, the PVA is burnt off totally at 500 to 550 °C for 3 h, and then the samples are sintered in air at 1135 to 1155 °C for 3 to 5 h. The top and bottom surfaces of the samples are coated with 5 to 15 % weight of silver paste and then fired at 700 to 750 °C for 10 min to form electrodes for the measurement of electrical properties. The *x* KNN_1+KNN_2+KNN_3 ceramics are processed in a silicon oil bath at 30 to 120 °C by applying a direct current (DC) electric field of 2 to 3 kV/mm for 15 to 20 min. The sample preparation process for the test dynamical mechanical analysis (DMA) is as follows: The *x* KNN_1+KNN_2+KNN_3 powders are thoroughly ground to form uniformly distributed particles with 8 *wt.*% PVA as a binder and then pressed into bar-shaped samples with a length of 10 - 10.5 mm, a width of 6 - 6.5 mm, and a thickness of 1.8 - 1.85 mm. The PVA is completely burnt off at 500 to 550 °C for 3 h, and subsequently, the samples are sintered in air at 1135 to 1155 °C for 3 to 5 h.

1.3 Characterization and measurement

The crystal structure and phase purity of the ceramics are confirmed by X-ray powder diffraction (XRD, Rigaku, D/Max2500, Tokyo, Japan). To confirm the distortion of the BO_6 octahedron and local heterogeneity in the ceramics, a Raman spectrometer or Raman mapping is used, respectively. Raman analysis/Raman imaging is done with a confocal Raman microscope (Alpha300R, WITec GmbH, Germany) equipped with a TEM single-frequency laser (λ = 532 nm, laser power = 40 mW, WITec GmbH, Germany). Surface morphology and energy-dispersive spectroscopy (EDS) mapping of the samples are examined using scanning electron microscopy of backscattered electrons (BSE-SEM, S-3400N, Hitachi, Japan). The average grain size (AGS) is analyzed from the BSE-SEM images using a Nanomeasurer program based on over 150 grains. The polished ceramic samples are cut into thin slices using a focused ion beam (FIB, Helios 5 CX, Thermo Scientific Company), and high-angle annular dark

field scanning transmission electron microscopy (HAADF-STEM) is performed using a Talos F200S G2 microscopy. A piezoelectric force microscopy (PFM) by a commercial microscope (MFP-3D, Asylum Research, Goleta, CA, USA) is used to characterize the domain structure. A precision impedance analyzer (TH2827, Tonghui Electronic Co, China) is used to measure the temperature dependence of the relative dielectric constant (ε_r-T) curves. Mechanical properties are characterized by DMA in three-point bending geometry using a Perkin Elmer DMA1 apparatus. DMA measurements are conducted at frequencies ranging from 0.5 to 10 Hz and at temperatures ranging from 30 to 500 °C. The ferroelectric TF Analyzer 2000 (aixACCT, Germany) is used to characterize the current (*I*-*E*) loops, the polarization *vs*. the electric field (*P*-*E*) behaviors, and the unipolar and bipolar strain *vs*. the electric field (*S*-*E*) loops. A quasi-static d_{33} meter (ZJ-3A, Institute of Acoustics, Chinese Academy of Sciences) is used for the d_{33} measurement of the ceramics. The *in-situ* temperature dependence of d_{33} is carried out by using a high-temperature piezometer (TZQD-D33T, China). The first radial mode frequencies (resonance frequency f_r and anti-resonance frequency f_a) are recorded by an LCR analyzer (Tonghui 2816A, China and HP 4980, Agilent). These parameters are also used to calculate the planar electromechanical coupling factor (k_p) and mechanical quality factor (Q_m) through the following formulas:[4]

$$k_p \approx \sqrt{2.51\frac{f_a - f_r}{f_a} - \left(\frac{f_a - f_r}{f_a}\right)^2} \quad (1)$$

$$Q_m = \frac{f_a^2}{2\pi f_r Z_m C^T \left(f_a^2 - f_r^2\right)} \quad (2)$$

2. **Results and discussion**

In Fig. S1(a), it is observed that the intensity ratio and position of the (002) and (200) Bragg peaks around 45°-46° are found to change with the addition of KNN_1, suggesting that multi-element are introduced into the A/B/O site of lattices affected the multiphase structure of the ceramics. It can be seen from Fig. 4(c) that at x = 0.05, 0.20, the tetragonal (T) and orthorhombic (O) phases at the rhombohedral-O-T (R-O-T)

phase boundary are predominant and the R phase is less because $T_{R\text{-}O}$ is much further away from room temperature, and similarly when $x = 0.40$, the R and O phases at the R-O-T phase boundary are comparatively more. A crystal structure model consisting of the R phase with a space group of *R*3*m*, the T phase with a space group of *P*4*mm*, and the O phase with a space group of *Amm*2 is used for pattern fitting to estimate the lattice distortion and volume fraction of the R, T, and O phases. The results of the Rietveld refinement for samples provided information on the crystal structure and phase structure, which are listed in Table S1. As x increases from 0.05 to 0.80, the volume fractions of the R, T, and O phases of the ceramics change with increasing $T_{R\text{-}O}$ and decreasing $T_{O\text{-}T}$. At room temperature, the dominant phase of $x = 0.20$ ceramics is a T phase with a volume fraction approximately equal to 50%, whereas the O phase dominates the $x = 0.05$ ceramics with a T phase approximately equal to 30%. It is found that the volume fractions of R, O, and T phases tend to be equal when $x \geq 0.40$.

A large T phase fraction can lead to stronger piezoelectricity in KNN ceramics. Z. Tan et al.[5] gave a detailed explanation of this behavior by modeling and calculating with the Order-Disorder theory (employing $KNbO_3$ as the model). That is, the piezoelectric constant has a positive correlation with the polarization change induced by constant stress. When external stress is applied, the internal ionic will rearrange to reduce the free energy of the system. In the R phase, the rearrangement of Nb is only realized by stretching or contracting the Nb-O bond, which is seriously resisted. In the O and T phases, the switchable Nb-O bond in a nonpolarized direction can re-bond, thus causing the transformation from order-disorder to order and giving rise to a huge change in polarization. This can be realized in 1 direction in the O phase and 2 directions in the T phase. Thus, the T phase is expected to have stronger piezoelectricity than the O phase, and both the T and O phases are stronger than the R phase. In addition, the d_{33} could be at high levels for all orientations in the tetragonal perovskite, while in orthorhombic and rhombohedral perovskites, the d_{33} is low in multiple directions, which deteriorates the average piezoelectric property in polycrystalline ceramics with O and R phases[6]. So, the T-rich phase at the R-O-T phase boundary is responsible for enhanced piezoelectricity.

The average ionic size and valence states difference (δ) is the parameter that is most commonly used to describe the lattice distortion, and the δ of the A-site, B-site, and O-site can be calculated as[7]:

$$\delta(R_A) = \sqrt{\sum_{i=1}^{n} c_i\left(1 - \frac{R_{A_i}}{\sum_{i=1}^{n} c_i R_{A_i}}\right)^2} \tag{3}$$

$$\delta(R_B) = \sqrt{\sum_{i=1}^{n} c_i\left(1 - \frac{R_{B_i}}{\sum_{i=1}^{n} c_i R_{B_i}}\right)^2} \tag{4}$$

$$\delta(R_O) = \sqrt{\sum_{i=1}^{n} c_i\left(1 - \frac{R_{O_i}}{\sum_{i=1}^{n} c_i R_{O_i}}\right)^2} \tag{5}$$

where R_{A_i}, R_{B_i}, and R_{O_i} is the ionic radius of the *i*th element at the A-site, B-site, and O-site, and c_i is the molar percentage of the *i*th ion.

$$\delta(V_A) = \sqrt{\sum_{i=1}^{n} c_i\left(1 - \frac{V_{A_i}}{\sum_{i=1}^{n} c_i V_{A_i}}\right)^2} \tag{6}$$

$$\delta(V_B) = \sqrt{\sum_{i=1}^{n} c_i\left(1 - \frac{V_{B_i}}{\sum_{i=1}^{n} c_i V_{B_i}}\right)^2} \tag{7}$$

$$\delta(V_O) = \sqrt{\sum_{i=1}^{n} c_i\left(1 - \frac{V_{O_i}}{\sum_{i=1}^{n} c_i V_{O_i}}\right)^2} \tag{8}$$

where V_{A_i}, V_{B_i}, and V_{O_i} is the valence states of the *i*th element at the A-site, B-site, and O-site, and c_i is the molar percentage of the *i*th ion.

Table S1. The crystal structure parameters and phase structure information of multiphase of

ceramics from the Rietveld structure refinement results.

x	0.05			0.20			0.40			0.80		
Sig	1.45			1.85			1.51			1.80		
R_w (%)	4.65			5.74			4.61			5.34		
Phase	R	T	O	R	T	O	R	T	O	R	T	O
content (%)	(13.2 2)	(33.3 2)	(53.4 4)	(17.7 3)	(48.9 0)	(33.3 6)	(33.9 2)	(27.2 9)	(38.7 8)	(30.2 8)	(31.2 4)	(38.4 6)
a (Å)	3.97 25	3.96 81	3.973 9	3.97 06	3.970 5	3.97 34	3.97 26	3.96 94	3.965 7	3.97 59	3.96 92	3.969 0
b (Å)	3.97 25	3.96 81	5.636 4	3.97 06	3.970 5	5.63 86	3.97 26	3.96 94	5.671 8	3.97 59	3.69 2	5.695 6
c (Å)	3.97 25	3.98 87	5.666 7	3.97 06	3.978 8	5.67 06	3.97 26	4.00 03	5.641 7	3.97 59	4.00 8	5.631 4
$\alpha = \beta = \gamma$ (°)	89.8 71	90	90	88.9 02	90	90	89.0 99	90	90	88.9 45	90	90

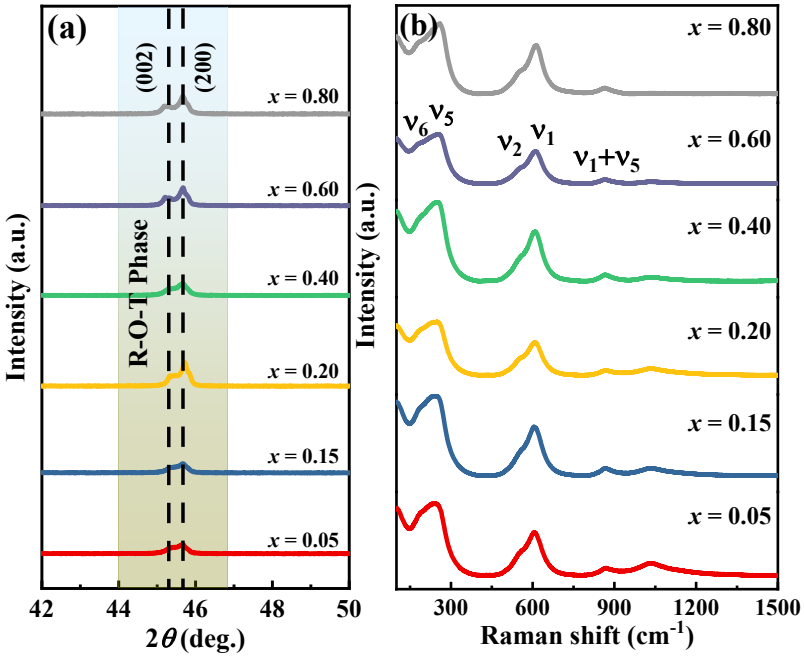

Fig. S1 (a) Amplified XRD patterns at $2\theta = 42^{\circ}$-50°. (b) Raman spectra of the ceramics.

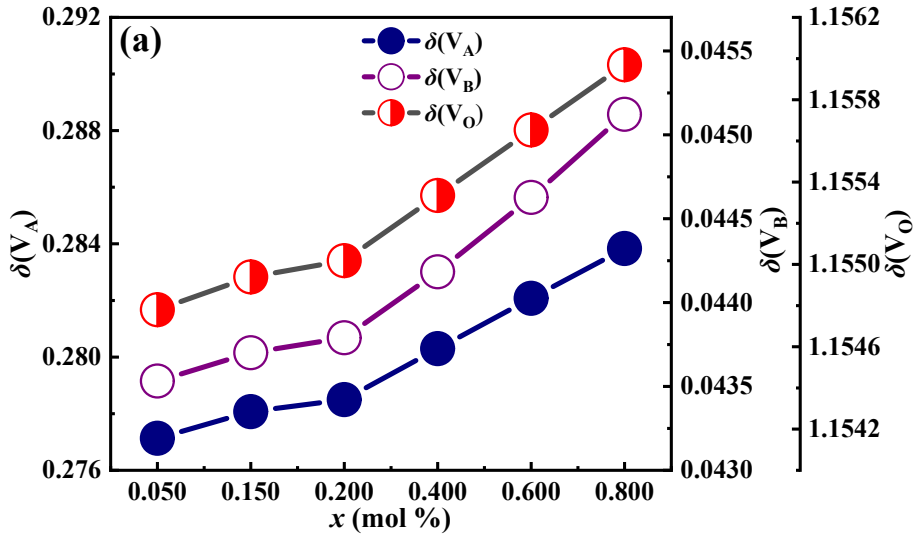

Fig. S2 (a) $\delta(V_A)$, $\delta(V_B)$, and $\delta(V_O)$ values of the samples as a function of x content.

The BSE-SEM images of ceramics are shown in Fig. S3. As x increases from 0.05 to 0.80, the AGS of ceramics shows a decreasing trend. Thanks to intrinsic disordered lattice distortion arising from disordered composition distribution. Intrinsic disordered lattice distortion leads to sluggish diffusion and fine grains[8]. The BSE-SEM image and corresponding elemental mappings of 0.20 KNN_1+KNN_2+KNN_3 ceramic are depicted in Fig. S4. The fact that all elements are uniformly distributed is further evidence that all elements enter the lattice to form a solid solution.

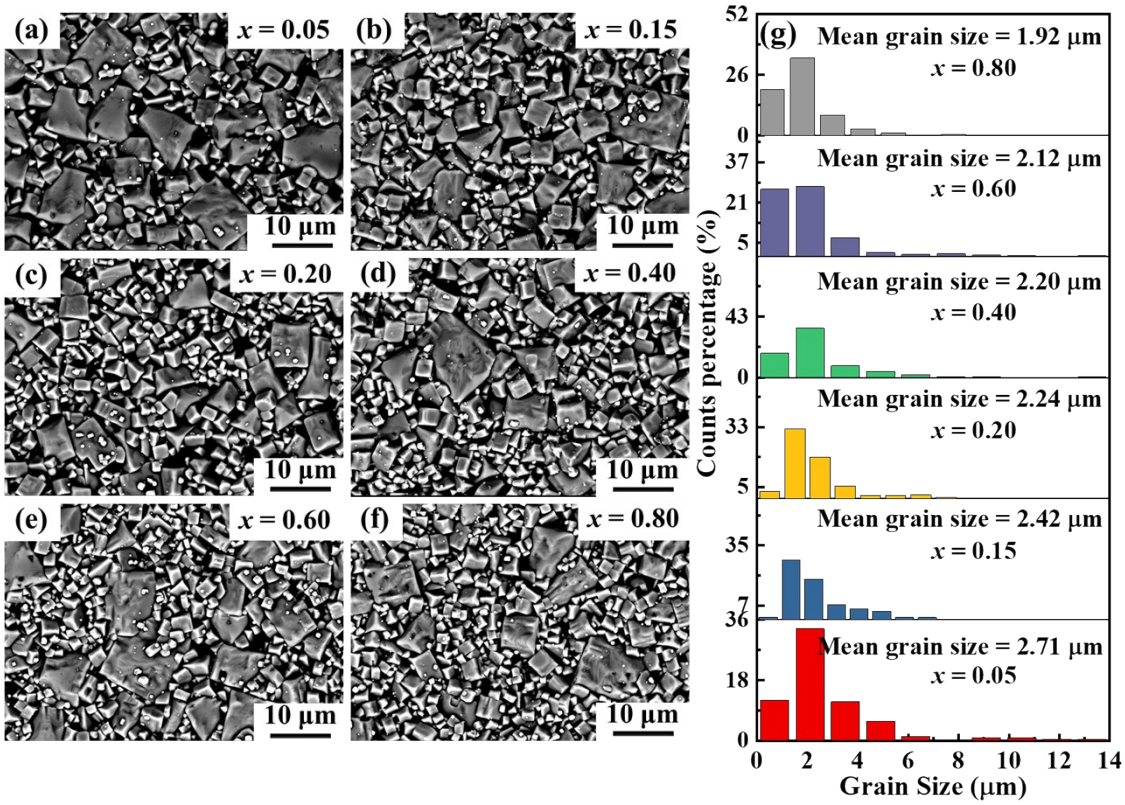

Fig. S3 (a)-(f) BSE-SEM images of the ceramics with different amounts of KNN_1; (g) grain size distribution of each image and variations in the average grain size of the samples.

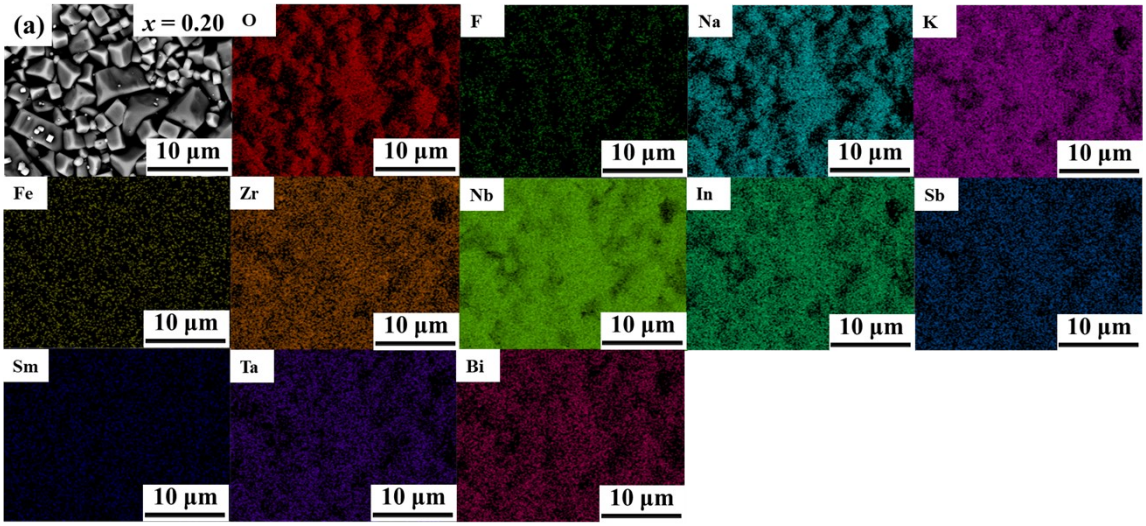

Fig. S4 (a) Mapping images of elemental for the 0.20 KNN_1+KNN_2+KNN_3 ceramic.

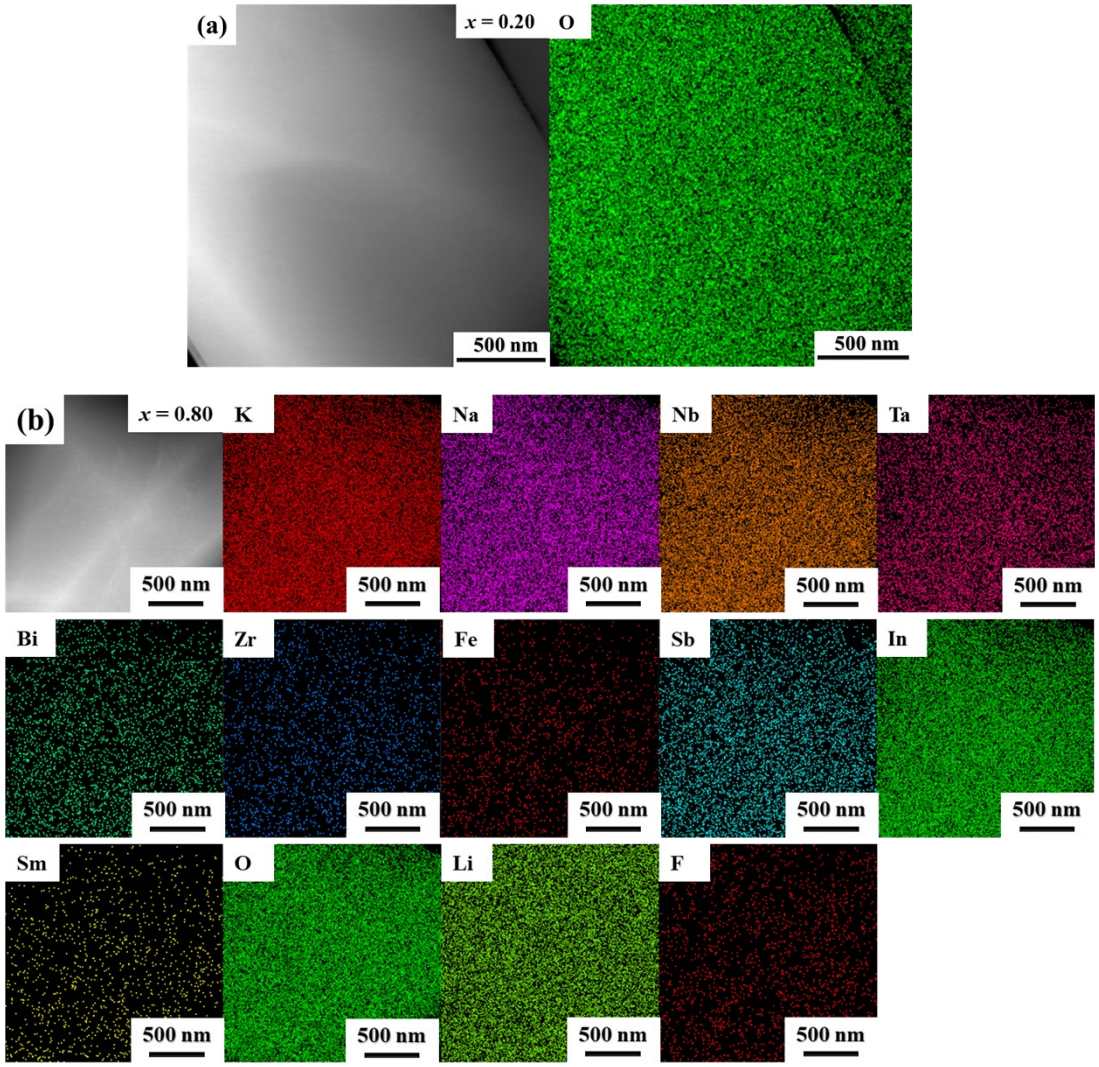

Fig. S5 HAADF-STEM image and EDS element mapping of (a) 0.20 KNN_1+KNN_2+KNN_3 and (b) 0.80 KNN_1+KNN_2+KNN_3 ceramic.

The above analyses are further verified through DMA. Mechanoelastic effects that might be associated with this phase sequence are investigated by DMA, a powerful technique for studying ferroelastic transitions, widely applied to ferroelectrics[9].

$$\sigma = \sigma_0 e^{i\omega t} \tag{9}$$

$$\varepsilon(t) = \varepsilon_0 e^{-i(\omega t + \delta)} \tag{10}$$

$$E^* = \frac{\sigma(t)}{\varepsilon(t)} = \frac{\sigma_0}{\varepsilon_0} e^{i\delta} = \frac{\sigma_0}{\varepsilon_0}(cos\delta + isin\delta) \tag{11}$$

$$E^* = |E^*|(cos\delta + isin\delta) = E' + iE'' \tag{12}$$

$$E^{'} = \frac{\sigma_0}{\varepsilon_0} cos\delta \tag{13}$$

$$E^{''} = \frac{\sigma_0}{\varepsilon_0} sin\delta \tag{14}$$

$$tan\delta = \frac{E^{''}}{E^{'}} \tag{15}$$

$$\left|E^{*}\right| = \sqrt{E^{'2} + E^{''2}} \tag{16}$$

The real part of the complex modulus E^*, E', represents the energy storage in the material due to elastic deformation during the deformation process, and is known as the energy storage modulus. It is measured under dynamic conditions and is different from the elastic modulus measured under static force conditions; the imaginary part E'' characterizes the energy loss as heat due to viscoelastic deformation during the deformation process, and is called the loss modulus; δ is the loss angle, and tanδ is the loss factor.

The E', tanδ, and E'' as a function of temperature for the x KNN_1+KNN_2+KNN_3 (x = 0.05, 0.20, and 0.80) ceramics are shown in Fig. S6 and Fig. 5(a-c). Generally, the modulus softens and minimizes at the phase transition point, so the phase transition characteristics of ferroelectric materials can be characterized by DMA. It is evident that with increasing temperature E' value first a slight increase, followed by a steep increase above T_C. Samples exhibit a local minimum of E' value in the vicinity of T_C. With a further increase in temperature, the rate of this increase gradually decreases until it levels off with peak values at the highest measurement temperature. It should be noted that the E' value of x KNN_1+KNN_2+KNN_3 (x = 0.05, 0.20, and 0.80) ceramics are much higher at a high temperature above 300 °C, i.e. in the paraelectric phase than at low temperature i.e. in the ferroelectric phases below 100 °C. This behavior is completely similar to other KNN-based ceramics[10, 11], barium titanate ceramics[12], and $BiMnO_3$-$BiFeO_3$-$PbTiO_3$ systems[9].

While the first slight increase during heating may be due to the closure (due to thermal expansion) of microcracks (which are the result of the thermal mismatch

stresses caused by the random orientation of non-spherical grains with anisotropic thermal expansion), the elastic anomaly (mechanical softening) at around 250 °C during heating is caused by the phase transition from the T to the cubic (C) phase[9]. However, the fact that E' does not change abruptly, when the T_C is exceeded during heating, must be attributed to the fact that upon exceeding the T_C ferroelectric behavior is not eliminated, which indicates that even in the high-temperature paraelectric phase certain remnants of ferroelectric domains survive. That means that the gradual increase of E' during heating above the T_C has nothing to do with microcrack closure. E' above T_C gradually increases and reaches a maximum value, which may be because the paraelectric C phase has a lower degree of lattice distortion than that of the ferroelectric R, O, and T phases under temperature conditions.

An anomaly characterized by a sudden softening and minimization of the E' at the T_C is observed during the heating process. The onset temperature of the elastic anomaly (mechanical softening) is lower than the temperature corresponding to the dielectric peak, which possibly originates from an intrinsic phase transition mechanism[11]. The elastic modulus is always the lowest for a given ferroelectric phase before the phase transition when the potential energy surface is at its lowest and flattest. The elastic modulus is at its lowest when the phase transition is about to take place. However, once the phase transition occurs, the C phase loses its ferroelectric polarization and corresponding strain, and then the elastic modulus rises rapidly. The reason why the elastic anomaly signals the onset of the ferroelectric to C phase transition instead of the average transition must be the sensitivity of E' to the ferroelectric/ferroelastic activity. Whereas the permittivity of perovskite systems is associated with the ordered-disordered phase transition mechanism. The phase transition from low to high temperatures always leads to an increase in the permittivity, and it is only after the phase transition occurs that the permittivity becomes higher. This phenomenon can be understood by the eight-site model, the B-site atom at a high-temperature phase can occupy more sites, and thus it is easier to induce electric polarization under an external electric field. The elastic anomalies signal the onset of the ferroelectric to C phase transition on heating, while the dielectric anomalies take place at the average

temperature[11].

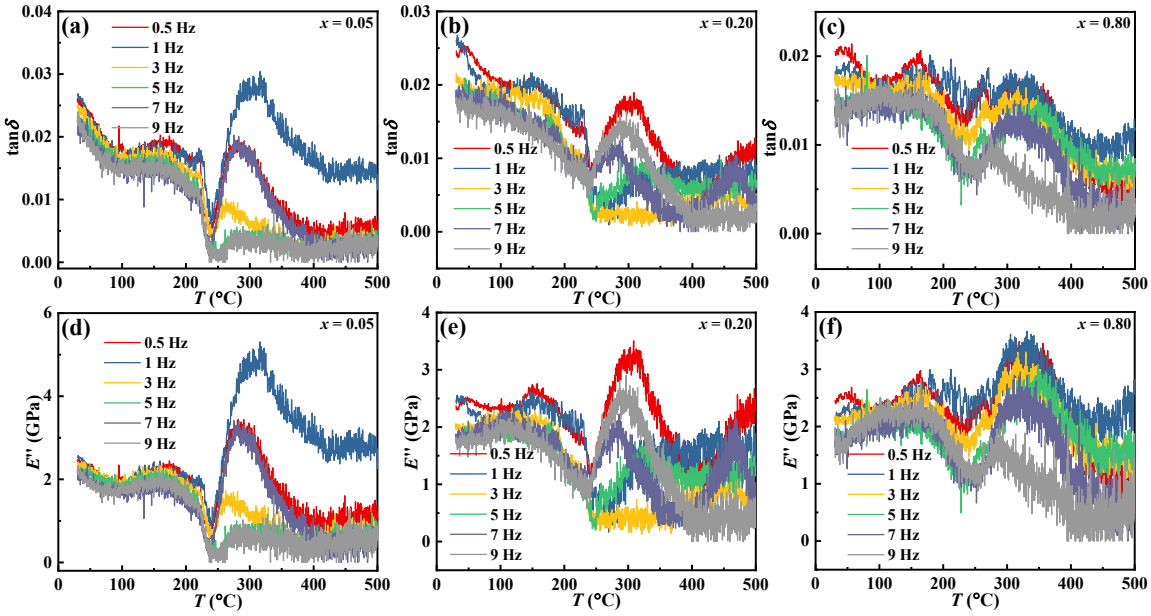

Fig. S6 The tanδ for (a) x = 0.05, (b) x = 0.20, and (c) x = 0.80. E'' for (d) x = 0.05, (e) x = 0.20, and (f) x = 0.80.

Fig. 8(c) presents the ε_r-T for x KNN_1+KNN_2+KNN_3 ceramics in the temperature range of 20 to 500 °C. The T_C of ceramics increases with the addition of KNN_1. The temperature-dependent dielectric properties of the x KNN_1+KNN_2+KNN_3 ceramics are analyzed using a modified Curie-Weiss law[13-15], as shown in Fig. S7(a-f). The diffuse-phase transition behavior of perovskite ferroelectrics can be expressed using this law, which relates the dielectric constant (ε) to temperature (T) and a constant (C). The modified Curie-Weiss law is shown in Equation (17).

$$\varepsilon = C/(T - T_0) \tag{17}$$

$$\Delta T_m = T_{cw} - T_m \tag{18}$$

$$\frac{1}{\varepsilon_r} - \frac{1}{\varepsilon_m} = \frac{(T - T_m)^\gamma}{C} \tag{19}$$

The change in diffuse phase transition behavior of the ceramics is evaluated using the values of ΔT_m and diffuseness index (γ)[16]. ΔT_m is the difference between the transition temperature (T_m) and the Curie-Weiss temperature (T_{cw}), as shown in

Equation (18). The γ is calculated using Equation (19), which relates the dielectric constants at the maximum (ε_m) and the transition (ε_r) temperatures to the temperature and the constant (C). Fig. S7(g) shows the $\log(\frac{1}{\varepsilon_r} - \frac{1}{\varepsilon_m})$ as a function of $\log(T\text{-}T_m)$ curves, which can be used to evaluate the diffuseness of the ceramics. Generally, polar nanoregions (PNRs) are believed to originate from the local structural heterogeneity induced by the nanoscale fluctuation of dipoles, which endow ferroelectrics with obvious frequency-dependent dielectric properties (*i.e.*, relaxor behavior)[17, 18]. The γ is used to describe the degree of relaxor: $\gamma = 1$ for normal ferroelectrics without short-range PNRs existence, and $\gamma = 2$ for ideal relaxor ferroelectrics without long-range ferroelectric domains. From Fig. S7(g), the values of the γ gradually decrease with an increasing x. The decrease in the PNRs with the increase of KNN_1 incorporation can be attributed to several factors. The test results of XRD, Raman, and DMA suggest that the hardening of the crystal structure is enhanced after introducing KNN_1. The hardening of the crystal structure limits the displacement of atoms and deformation of lattice in the crystal, affecting the formation of PNRs. In addition, Ta and Nb have a similar distribution of electrons outside the nuclei of the atoms, and Ta replaces Sb which contributes to the long-range ferroelectric ordering. This inhibits the formation of high-density nanodomains along with PNRs, resulting in a reduction of relaxation behavior.

The *I-E* loops for the x KNN_1+KNN_2+KNN_3 ceramics are shown in Fig. 8(f). With the increase of the content of KNN_1, the peak of the *I-E* loops first becomes sharp and then becomes flat, and the optimal value is obtained at $x = 0.2$. This indicates that the addition of an appropriate amount of the KNN_1 can promote domain-switching behavior in ceramics. In addition, it can be observed from the test results of ε_r-T curves and *P-E* loops that when the doping amount of KNN_1 is 0.2, P_r can be increased while maintaining a high level of ε_r. Based on the above phenomenon, it can be speculated that when the doping amount of KNN_1 is 0.2, it may be the optimal PNRs content.

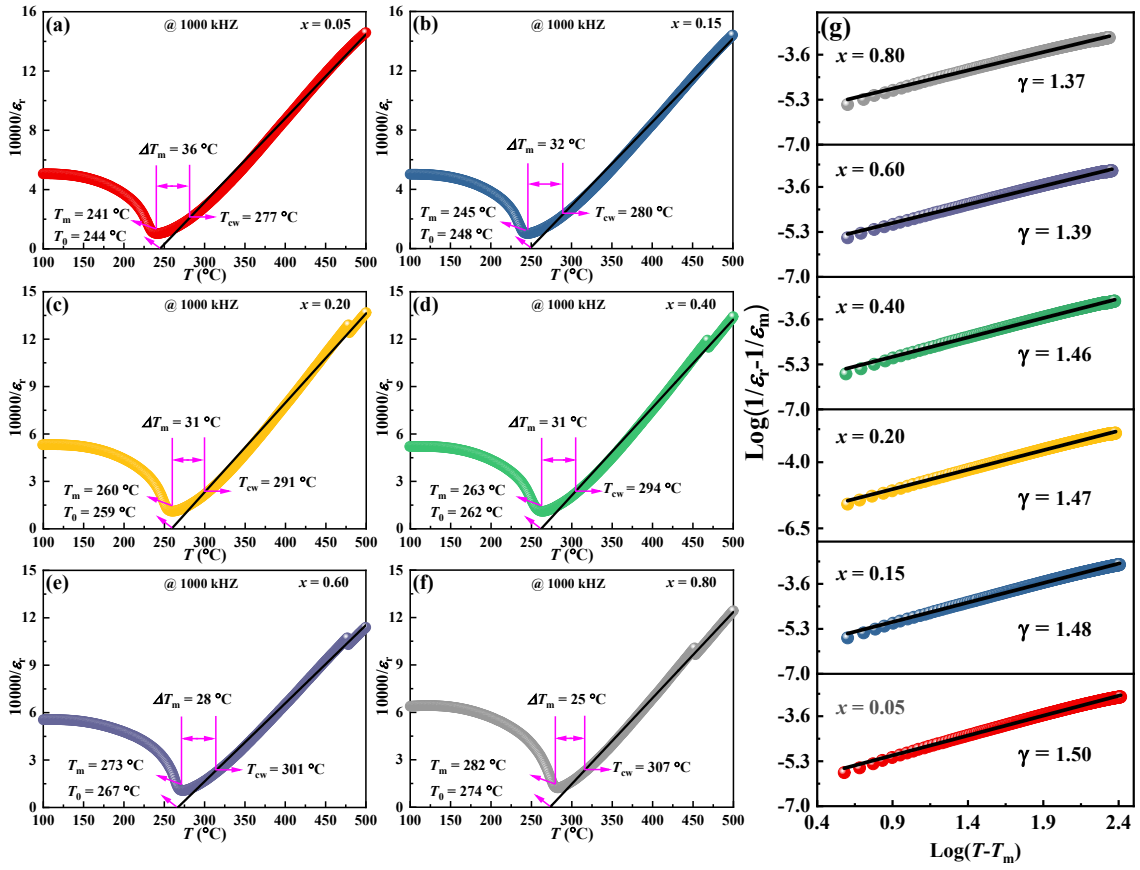

Fig. S7. (a)-(f) The relationship of the temperature and inverse dielectric permittivity of ceramics; (g) a plot of $\log(\frac{1}{\varepsilon_r} - \frac{1}{\varepsilon_m})$ as a function of $\log(T\text{-}T_m)$ for ceramics, and composition dependence of γ of the ceramics.

The relationship between grain size and domain size in perovskite-structure polycrystalline piezoelectrics can be described as follows[19]:

$$Domain\ size \propto (grain\ size)^m \tag{20}$$

where m is an exponent. When grain size is in the range of 1-10 μm, m approaches 1/2; when grain size is larger than 10 μm, m is in the range of 0-1/2, and when grain size is smaller than 1 mm, m is in the range of 1/2-1[19]. It is easy to understand this empirical equation. When progressively reducing the grain size, the whole grain will only contain one domain or even less than one domain, indicating m approaches 1. When monotonously increasing the grain size, the domain cannot follow a monotonous increase due to the free energy of the system, the internal stress, and the coupling of domains and grains, resulting in an m of less than 1/2. In this work, it can be seen from

Fig. S3 that the morphology of the ceramics is characterized by small grains surrounding large grains. Grains of types larger than 10 μm, within the range of 1-10 μm, and smaller than 1 mm all exist in the ceramics. This phenomenon can be explained in terms of energy. Large grains can easily accommodate several typical domains coexisting. However, as the grain size decreases, e.g., to 1.4 times the size of a typical domain, the energy required to form a single domain may become lower than that required to form two smaller coexisting domains, which could give rise to the formation of larger domains. Additionally, the electron distribution of Ta and Nb outside the atomic nucleus is similar. The substitution of Sb by Ta contributes to long-range ferroelectric ordering, thereby increasing the domain size. This might be the reason why the AGS of the ceramics shows a decreasing trend, while the domain size of the ceramics has an increasing trend.

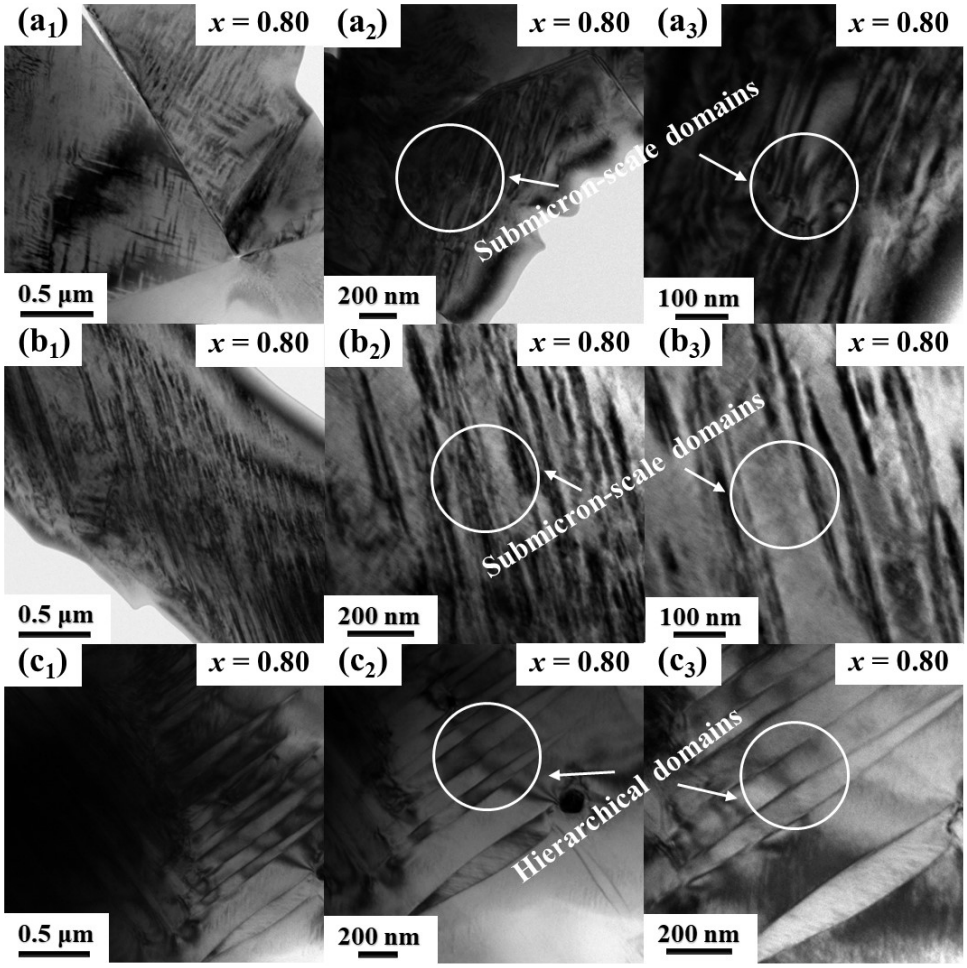

Fig. S8. Domain configurations of the 0.80 KNN_1+KNN_2+KNN_3 ceramic. (a_2-a_3), (b_2-b_3), and (c_2-

c_3) are enlarged views of localized areas of (a_1), (b_1), and (c_1), respectively.

The *S-E* curves are displayed in Fig. S9(a). The unipolar strain (S_{uni}) gradually decreases with increasing KNN_1 content. The reverse piezoelectric coefficients ($d^*_{33} = S_{max}/E_{max}$) as a function of KNN_1 content, which decreases from 597 pm/V to 441 pm/V. The decreased S_{uni} and d^*_{33} values of the ceramics are mainly due to the increase in the intrinsic disordered lattice distortion, which can limit the strain response. Fig. S9(b) demonstrates that a simultaneous increase in k_p and Q_m can be achieved through the synergistic action of KNN_1, KNN_2, and KNN_3. The k_p of the ceramics first increases to a maximum value of 0.55 and then considerably reduces with the addition of KNN_1. The Q_m of the ceramics increases with x increases. For device applications, the temperature stability of piezoelectric properties is an important factor to consider. In this study, the *in-situ* temperature-dependent d_{33} of the ceramics are measured, and the results are presented in Fig. S9(c). It can be seen from Fig. S9(c) that the KNN_1 system has better d_{33} temperature stability compared with the KNN_2 and KNN_3 systems. With the addition of KNN_1, not only T_C is increased, but also the d_{33} temperature stability of the 0.2 KNN_1 + KNN_2 + KNN_3 ceramics is improved compared with the KNN_2 and KNN_3 systems.

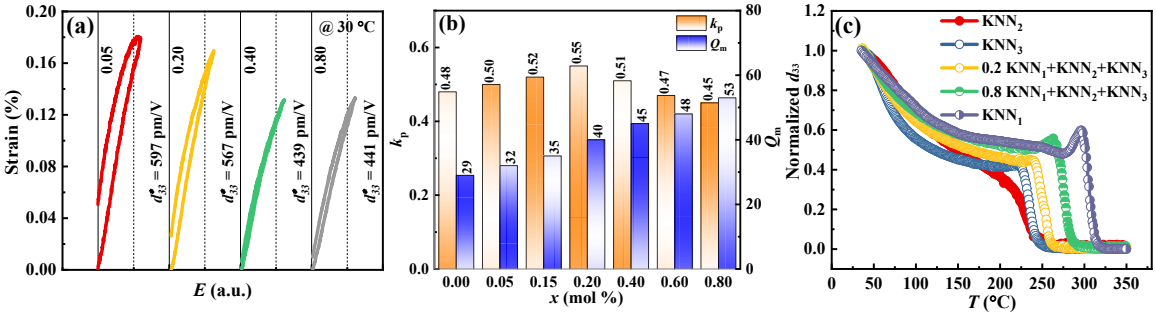

Fig. S9. (a) Unipolar *S-E* curves of ceramics. (b) k_p and Q_m values as a function of KNN_1 content. (c) *In-situ* temperature stability of d_{33} for KNN_1, KNN_2, KNN_3, 0.20 KNN_1+KNN_2+KNN_3, and 0.80 KNN_1+KNN_2+KNN_3 ceramic.

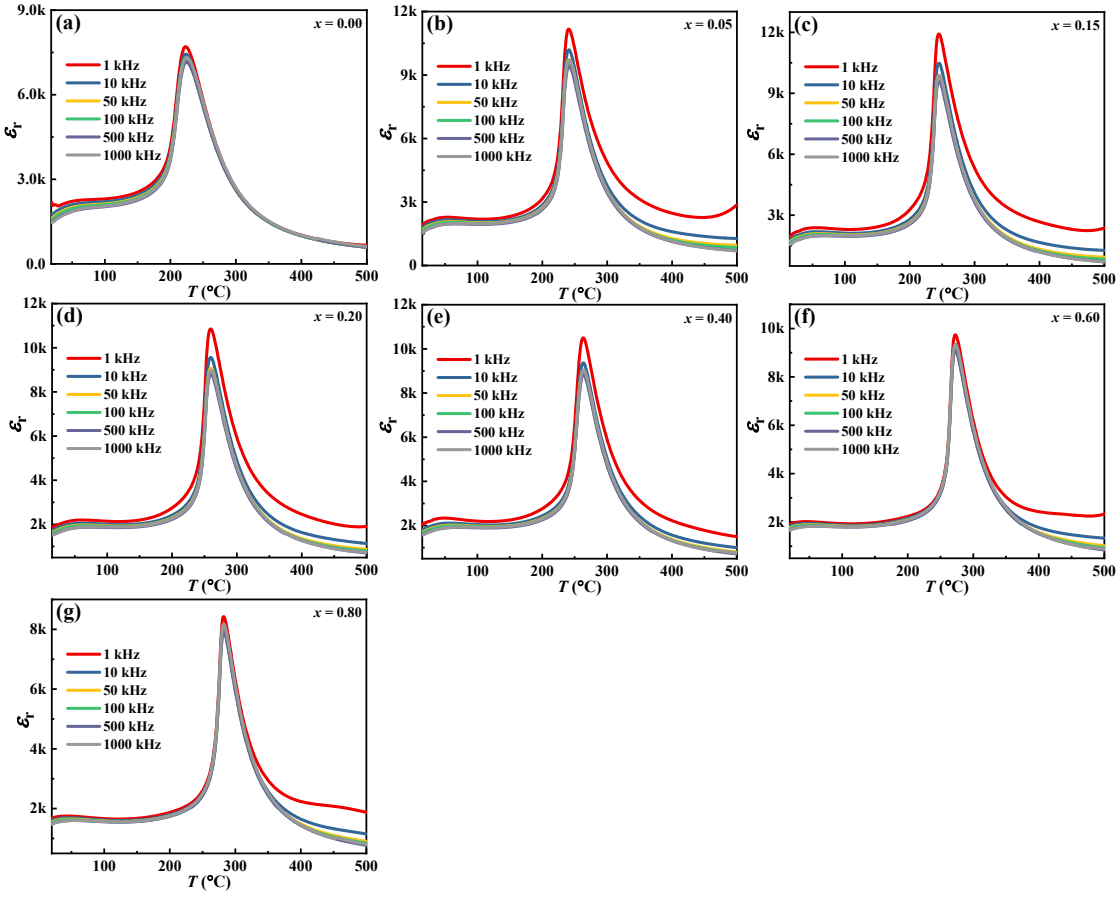

Fig. S10. ε_r-T curves for x KNN_1+KNN_2+KNN_3 ceramics in the temperature range from 30 to 500 °C.

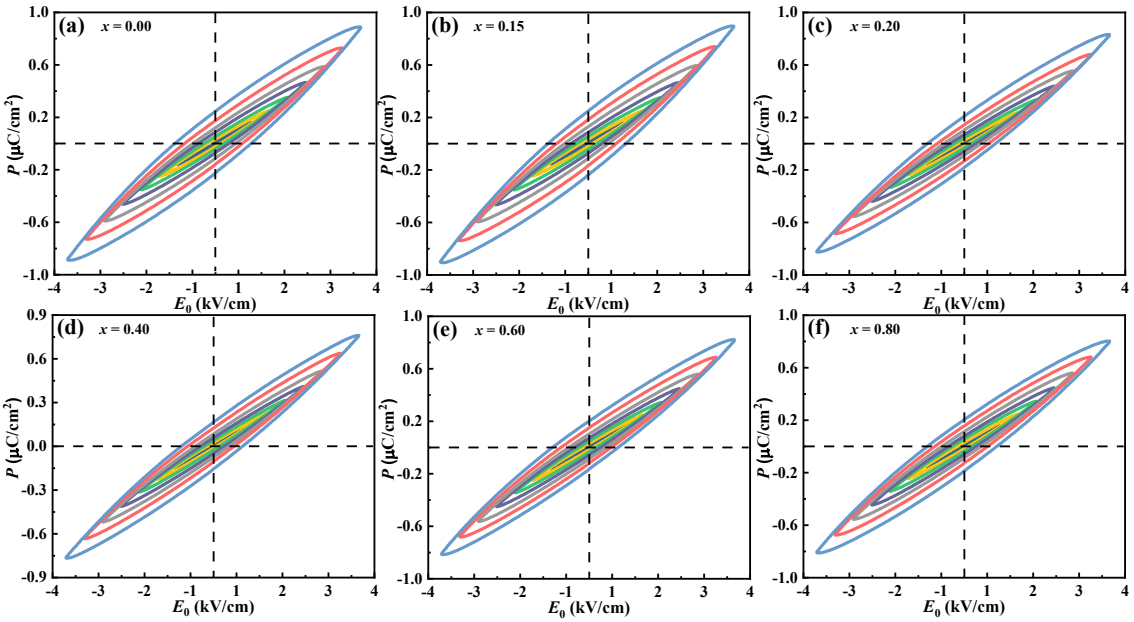

Fig. S11 (a-g) shows typical P-E curves in the sub-coercive field region for the x KNN_1+KNN_2+KNN_3 ceramics.

References

1. H. Li, N. Chen, J. Xing, H. Chen, Z. Tan, M. Mo, Q. Chen, J. Zhu, F. Li, Z. Liu, W. Ouyang and H. Zhu, *Journal of Materials Chemistry C*, 2024, 12, 1809-1819.
2. Y. Cheng, J. Xing, X. Li, L. Xie, Y. Xie, Z. Tan and J. Zhu, *Journal of the American Ceramic Society*, 2022, 105, 5213-5221.
3. C. Shi, J. Ma, J. Wu, X. Wang, F. Miao, Y. Huang, K. Chen, W. Wu and B. Wu, *Journal of Alloys and Compounds*, 2020, 846, 156245.
4. S. Zhang, E. F. Alberta, R. E. Eitel, C. A. Randall and T. R. Shrout, *Ieee Transactions on Ultrasonics Ferroelectrics and Frequency Control*, 2005, 52, 2131-2139.
5. Z. Tan, Y. Peng, J. An, Q. Zhang and J. Zhu, *Inorganic Chemistry*, 2021, 60, 7961-7973.
6. X. Gao, Z. Cheng, Z. Chen, Y. Liu, X. Meng, X. Zhang, J. Wang, Q. Guo, B. Li, H. Sun, Q. Gu, H. Hao, Q. Shen, J. Wu, X. Liao, S. P. Ringer, H. Liu, L. Zhang, W. Chen, F. Li and S. Zhang, *Nature Communications*, 2021, 12, 881.
7. L. Chen, H. Yu, J. Wu, S. Deng, H. Liu, L. Zhu, H. Qi and J. Chen, *Nano-Micro Letters*, 2023, 15, 65-79.
8. Y. Zhang, L. Chen, H. Liu, S. Deng, H. Qi and J. Chen, *InfoMat*, 2023, 5, e12488.
9. C. M. Fernández-Posada, A. Castro, J.-M. Kiat, F. Porcher, O. Peña, R. Jiménez, M. Algueró and H. Amorín, *Advanced Functional Materials*, 2018, 28, 1802338.
10. S. Hříbalová, L. Kotrbová, E. Gregorová, A. Mašlová, V. Nečina, P. Šimonová and W. Pabst, *Journal of the European Ceramic Society*, 2024, 44, 6501-6509.
11. A. M. Mazuera, P. S. Silva, A. D. Rodrigues, P. S. Pizani, Y. Romaguera-Barcelay, M. Venet and M. Algueró, *Physical Review B*, 2016, 94, 184101.
12. W. Pabst, E. Gregorová, P. Šimonová and T. Uhlířová, *Ferroelectrics*, 2023, 611, 171-187.
13. J. Xing, S. Xie, B. Wu, Z. Tan, L. Jiang, L. Xie, Y. Cheng, J. Wu, D. Xiao and J. Zhu, *Scripta Materialia*, 2020, 177, 186-191.
14. J. Xing, Z. Tan, L. Xie, L. Jiang, J. Yuan, Q. Chen, J. Wu, W. Zhang, D. Xiao and J. Zhu, *Journal of the American Ceramic Society*, 2018, 101, 1632-1645.
15. M.-H. Zhang, Q. Zhang, T.-T. Yu, G. Li, H.-C. Thong, L.-Y. Peng, L. Liu, J. Ma, Y. Shen, Z. Shen, J. Daniels, L. Gu, B. Han, L.-Q. Chen, J.-F. Li, F. Li and K. Wang, *Materials Today*, 2021, 46, 44-53.
16. X. Ren, Z. Peng, B. Chen, Q. Shi, X. Qiao, D. Wu, G. Li, L. Jin, Z. Yang and X. Chao, *Journal of the European Ceramic Society*, 2020, 40, 2331-2337.
17. F. Li, S. Zhang, D. Damjanovic, L.-Q. Chen and T. R. Shrout, *Advanced Functional Materials*, 2018, 28, 1801540.
18. G. Xu, J. Wen, C. Stock and P. M. Gehring, *Nature Materials*, 2008, 7, 562-566.
19. W. Cao and C. A. Randall, *Journal of Physics and Chemistry of Solids*, 1996, 57, 1499-1505.